Using Computational Flow Imaging to Optimize Filtered Rayleigh Scattering Measurements of an Isolator Shock Train

Robin L. Hunt, Cody R. Ground, Robert A. Baurle, Paul M. Danehy
NASA Langley Research Center, Hampton, VA, 23681

Filtered Rayleigh scattering (FRS) is a laser diagnostic where the intensity of elastically scattered light is measured after it passes through a molecular absorption filter. The filter removes background interference that overwhelms the relatively weak scattering from the gas molecules. However, with a filter, the measured light intensity depends on many of the scattering gas properties, including pressure, density, temperature, and velocity. In this work, CFD simulations of an isolator shock train flow field are input into a physics-based model to predict the values of FRS intensity measurements in a proposed experiment. The goal is to evaluate if a simplistic FRS setup (that utilizes one camera, laser, and absorption filter) can be used to accurately quantify number density despite the fact that the scattered light intensity also depends on other gas properties. It is found that the experimental setup can be optimized such that a linear relationship describes the number density with an average prediction error of 2%. The vast majority of the flow exhibits prediction errors of less than 3%, but small regions of the flow reach up to 11% error. A sensitivity analysis shows that the prediction error increases with the central wavelength of the incident laser light and decreases with the angle between the camera and laser propagation directions. The optimal experimental parameters are chosen based on a compromise between the prediction error, spatial resolution, and the amount of unfiltered light. In the future, the proposed FRS setup will be implemented to acquire new and valuable information on an isolator shock train, a flow field that has been traditionally studied using wall static pressure measurements and path-integrated visualization techniques, such as schlieren and shadowgraphy.

Nomenclature

B	= Optical efficiency constant	p	= Pressure
c	= Speed of light	r	= Spectral profile of the RB scattered light prior to the absorption filter
c_{int}	= Dimensionless internal specific heat		
c_{tr}	= Dimensionless translational specific heat	T	= Temperature
$\frac{d\sigma}{d\Omega}$	= Differential scattering cross section	t	= Transmission spectrum of the absorption filter
E	= Total radiant energy measured by the camera	$\vec{v}$	= Velocity (vector) of the scattering gas
E_b	= Energy of the filtered background interference	W	= Isolator width, 50.80 mm
E_i	= Incident laser energy	x	= Streamwise coordinate direction
E_r	= RB scattered light energy after passing through the absorption filter	y	= Transverse coordinate direction
		z	= Vertical coordinate direction
H	= Isolator height, 25.40 mm	$\Delta\nu_D$	= Doppler shift
k	= Thermal conductivity	$\Delta\Omega$	= Solid angle over which the FRS camera lens collects light
$\hat{\mathcal{L}}$	= Unit vector in the laser propagation direction		
L_{cell}	= Optical length of the filter cell	η	= Shear viscosity
ℓ	= Laser sheet thickness in the direction of $\hat{\mathcal{O}}$	η_b	= Bulk viscosity
m	= Mass of a single molecule	θ	= Angle between $\hat{\mathcal{O}}$ and $\hat{\mathcal{L}}$
N	= Number density	ν	= Frequency
n	= Index of refraction	ν_c	= Central laser frequency
$\hat{\mathcal{O}}$	= Unit vector in the direction of the FRS camera	ρ_0	= Normal depolarization factor for natural light
$\hat{\mathcal{P}}$	= Unit vector in the laser polarization direction	ϕ	= Angle between $\hat{\mathcal{P}}$ and $\hat{\mathcal{O}}$

Subscripts

atm	=	Atmospheric value
cell	=	Gas conditions in the filter cell
inf	=	Isolator inflow condition (at $x = 0$)
pred	=	"Predicted" value derived from linear fit
truth	=	"True" value from CFD

Acronyms

CFD	=	Computational Fluid Dynamics
CFI	=	Computational Flow Image
FRS	=	Filtered Rayleigh Scattering
IDRL	=	Isolator Dynamics Research Laboratory
PCA	=	Principal Component Analysis
RANS	=	Reynolds-Averaged Navier-Stokes
RB	=	Rayleigh-Brillouin

I. Introduction

The isolator is a critical component in hypersonic air-breathing engines that connects the inlet to the combustor. In the lower hypersonic regime between flight Mach numbers 3 and 7, the heat-release in the combustor generates a series of coupled shock waves in the isolator, collectively called the shock train. If the isolator is too short then these shock waves may negatively interact with the inlet flow field leading to inlet unstart. However, an excessively long isolator has a weight and drag penalty. Thus, a thorough understanding of the shock train structure and dynamics is needed to design a minimal length isolator that contains the entire shock system during normal operation. The quantification and prediction of the isolator shock train flow field is particularly challenging because it is dominated by large separation regions and multiple shock/boundary layer interactions. This makes high-resolution, time-dependent computational fluid dynamics (CFD) simulations of the isolator shock train costly to acquire. CFD results are also sensitive to modeling choices, such as the turbulence model, making accurate predictions difficult to achieve [1–3]. Experimentally, advanced laser diagnostics are a desirable tool to study isolator shock trains because they can provide quantitative planar or volumetric measurements. Such measurements are needed to validate CFD models and can provide a holistic understanding of the large, complex shock system [4, 5].

The Isolator Dynamics Research Laboratory (IDRL) at the NASA Langley Research Center is currently configured as a Mach 2.5 cold flow, direct-connect isolator model designed for fundamental shock train research studies broadly motivated by the above discussion. It is intended to provide accurate and repeatable data of the isolator flow field using traditional high-speed wall pressure measurements, schlieren, and advanced laser diagnostics. One desired laser diagnostic is filtered Rayleigh scattering (FRS), a technique where the intensity of predominantly elastically scattered light is measured after it passes through a molecular absorption filter. FRS is a relatively simple yet powerful planar measurement technique that can provide spatially and temporally-resolved quantitative information. Thus, it is an ideal tool to study the detailed instantaneous flow structure of the isolator shock train. Such information extends our knowledge of this complex flow field past the wall-pressure measurements and path-integrated visualization techniques (such as schlieren and shadowgraphy) that have been traditionally used. Of particular interest is FRS measurements on cross-sectional planes in the isolator to study any asymmetry in the isolator shock front. In addition, the quantitative information gathered using FRS is an ideal way to validate CFD methods. While the quantification of only one flow property is discussed in this work, FRS can be extended or used simultaneously with other diagnostics to fully characterize the state of the flow. Another major benefit of FRS is that gas molecules will scatter the light so the flow does not have to be seeded, making it a truly nonintrusive technique. Without a filter, light intensity measurements are directly proportional to the scattering gas number density, N. However, the small-scale and enclosed nature of the IDRL flow field will result in significant background interference as the incident laser light also scatters off the facility walls and structural frame. This unwanted scattering can overwhelm the relatively weak signal from the scattering gas. Using a filter reduces this background interference, but the measured light intensity becomes a complex function of many parameters, including the pressure, number density, temperature, and velocity of the scattering gas.

In this work, CFD simulations of the IDRL shock train flow field are input into a physics-based model in order to predict the values of FRS intensity measurements in a proposed experiment. The two-dimensional image produced by extracting a single plane from the computed light intensity matrix, called a computational flow image (CFI), essentially predicts the signal that a camera would capture in an FRS experiment. The goal of this exercise is to evaluate if a single, simplistic FRS setup (that utilizes one camera, laser, and absorption filter) can be used to accurately quantify number density in this specific isolator flow field despite the fact that the scattered light intensity depends on many parameters. If successful, the proposed FRS setup will be implemented to gather new and valuable information on the isolator shock train.

II. Fundamentals of Filtered Rayleigh Scattering

Spontaneous Rayleigh-Brillouin (RB) scattering is the elastic scattering of light by molecules and nanoparticles, yielding the central Cabannes line in the spectral profile. In a typical RB scattering experiment, a laser beam or sheet illuminates a desired portion of the flow field and some of the light is scattered. The intensity and spectral profile of the scattered light contain information about the the flow properties. For example, the scattered light is shifted in frequency due to the Doppler effect, where the magnitude of the shift is related to the gas velocity. If the scattering gas is composed of molecules, the scattered light is also thermally broadened and its spectral profile is related to the gas pressure and temperature. When measured directly, the intensity of RB scattered light is proportional to the gas number density. However, these direct measurements suffer from background interference caused by scattering from walls and windows. Unlike the RB scattered light, the background scattering is not Doppler shifted or broadened, thus it has a similar spectral profile as the incident laser light. If the spectral lineshape of the background scattering overlaps that of the RB scattered light, both are captured in measurements. This interference can overwhelm the relatively weak scattering from the gas molecules. The FRS technique employs a molecular absorption filter between the gas sample and the camera in order to mitigate the background interference. Typically, the filter is a glass cell containing an atomic or molecular species, such as iodine. The absorption process acts as a notch filter so that the radiant energy of the background scattering is not captured in measurements. However, part of the RB scattering signal may also be filtered out.

The general FRS optical arrangement is shown in figure 1. An incident laser sheet, with a given spectral distribution, propagates in the $\hat{\mathcal{L}}$ direction. The laser polarization is in the $\hat{\mathcal{P}}$ direction. Light scattered in the $\hat{\mathcal{O}}$ direction passes through a filter and is then collected by a camera. The total radiant energy, E, that reaches a single resolution element of the camera sensor is equal to

$$E = E_r + E_b \tag{1}$$

where E_r is the energy of the RB scattered light after passing through the absorption filter and E_b is the energy of the background interference that is not removed by the filter. Ideally, E_b is close to zero and E_r is the primary contributor to the total radiant energy. The radiant energy collected by a single resolution element of the camera sensor is proportional to the pixel intensity. The same process occurs at all the other elements of the sensor to create an image of the measurement plane.

For cases where a pulsed laser is used, with radiant light collected over the duration of the pulse, the measured energy contribution of the RB scattered light is equal to

$$E_r = BN\ell E_i \frac{\mathrm{d}\sigma}{\mathrm{d}\Omega}(\hat{\mathcal{O}}, \hat{\mathcal{P}}, \nu_c, N, n, \rho_0)\Delta\Omega \left[\int_{-\infty}^{+\infty} t(\nu, p_{\mathrm{cell}}, T_{\mathrm{cell}}, L_{\mathrm{cell}}) r(\nu - \nu_c - \Delta\nu_D, \theta, T, p, m, \eta, \eta_b, k, c_{\mathrm{tr}}, c_{\mathrm{int}}) \mathrm{d}\nu \right] \tag{2}$$

where B is a constant that describes the optical efficiency, N is the number density of the scattering gas, ℓ is the laser sheet thickness (in the $\hat{\mathcal{O}}$ direction), E_i is the incident laser energy, $\Delta\Omega$ is the solid angle over which the sensor element

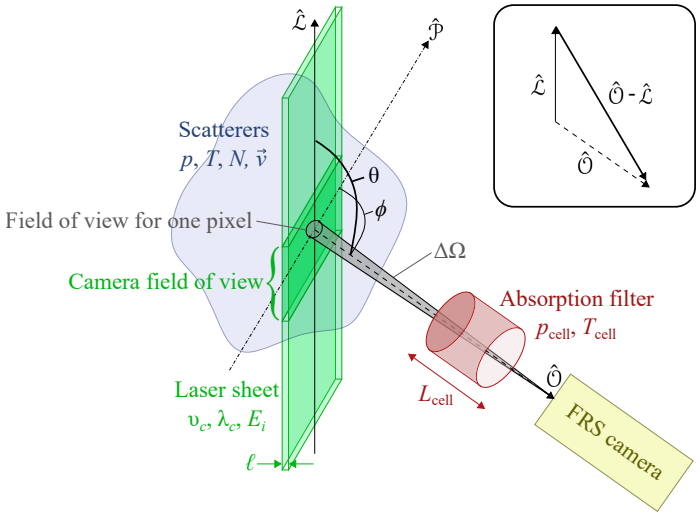

Fig. 1 Schematic diagram of a general FRS optical arrangement.

collects light, and $d\sigma/d\Omega$ is the differential scattering cross section. The differential scattering cross section is a complex function of the observation and polarization directions ($\hat{\mathcal{O}}$ and $\hat{\mathcal{P}}$, respectively), the central frequency of the incident laser light (ν_c), the number density (N), the index of refraction (n), and the normal depolarization factor for natural light (ρ_0). The product of terms within the integral of equation 2 describes the RB spectral lineshape after passing through the filter. The first term, t, is the transmission spectrum of the filter (normalized such that $t = 1$ when none of the light is absorbed and $t = 0$ when all of the light is absorbed by the filter). The second term, r, is the spectrum of the RB scattered light prior to the filter, which is normalized so that the integral over all frequencies is equal to one. When the product of t and r is integrated over all optical frequencies, the result describes the proportion of RB scattered radiant energy that reaches the observer (i.e., the camera). If no filter is present, this integral equals one and the total energy is directly proportional to the number density. When a filter is used, the integral term in equation 2 (and therefore the total energy) depends on properties of the scattering gas, the optical arrangement, the laser, and the filter. Specifically, t is a function of frequency (ν), the pressure of the filter gas (P_{cell}), the temperature of the filter gas (T_{cell}), and the optical length of the filter (L_{cell}). The angle between the RB scattered light and filter face also weakly influences the transmission. In this work, it is assumed that the RB scattered light passing through the filter is approximately perpendicular to the filter face and thus, this angle dependence is negligible. The second term in the integral, r, depends on the properties of the scattering gas, including its temperature (T), pressure (p), shear viscosity (η), bulk viscosity (η_b), thermal conductivity (k), dimensionless internal and translational specific heat capacities (c_{int} and c_{tr}, respectively), and the particle mass (m). In addition to the gas properties, r is a function of the frequency (ν), the central laser frequency (ν_c), the scattering angle (θ, defined as the angle between $\hat{\mathcal{L}}$ and $\hat{\mathcal{O}}$), and the Doppler shift ($\Delta\nu_D$). The Doppler shift is caused by the bulk fluid motion of the scattering particles, $\vec{v}$, and is equal to

$$\Delta\nu_D(\theta, \vec{v}) = \frac{\nu_c \vec{v}}{c} \bullet \left(\hat{\mathcal{O}} - \hat{\mathcal{L}}\right) \tag{3}$$

where c is the speed of light.

Figure 2 summarizes the FRS calculations using simulated spectra. In this example, the incident laser light is tuned such that its entire lineshape (blue curve) falls in the center of a strong absorption line (red curve). Thus, the incident laser light and background scattering are removed from the measurement. The unfiltered RB scattering lineshape (black curve) is Doppler shifted and thermally broadened. Some of the RB scattered light is absorbed as it passes through the filter and the remaining light is detected by the camera. The camera does not distinguish different frequencies of light, therefore the measurement is proportional to the integral of the filtered RB scattering lineshape over all frequencies (green shaded region).

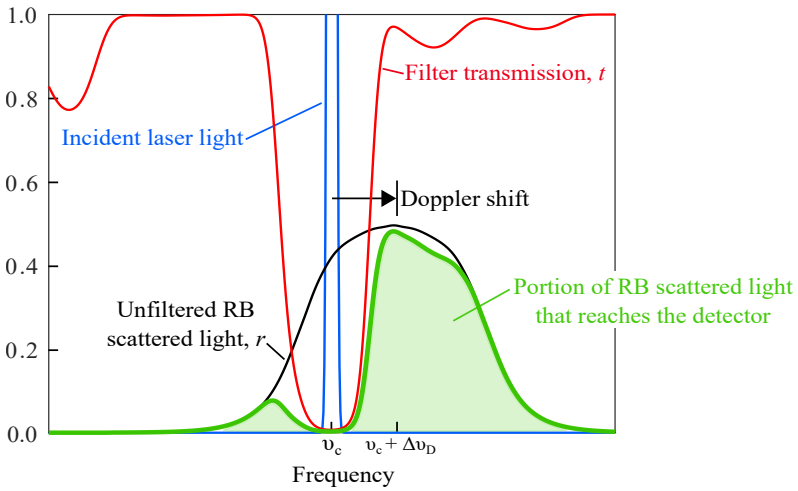

Fig. 2 Simulated spectra that demonstrate how an absorption cell filters out the light from background scattering (which has a similar spectrum as the incident laser light). Part of the RB scattered light is also filtered out. Computations made using: $p_{\text{cell}} = 100$ **Pa,** $T_{\text{cell}} = 300$ **K,** $L_{\text{cell}} = 9$ **cm,** $\nu_c = 563.1488$ **THz,** $\Delta\nu_D = 939.2312$ **MHz (or 500 m/s),** $p = 101.325$ **Pa, and** $T = 298.15$ **K.**

III. Proposed FRS Experiment

The proposed experiment utilizes FRS to study the shock train flow field in the Isolator Dynamics Research Laboratory (IDRL). The IDRL is a cold flow, direct-connect isolator model at the NASA Langley Research Center. The key components of the facility are schematically illustrated in figure 3. Unheated, dry air from a compressed air line is used to supply the plenum section. Up to 1.8 kg/s of air is accelerated through a two-dimensional Mach 2.5 nozzle. The air then enters a 695.71 mm long isolator with a constant area cross-section that measures 50.80 × 25.40 mm (width, W × height, H). Glass walls provide wall-to-wall optical access along 609.60 mm of the isolator length. The origin of the right-handed coordinate system is located at the beginning of the isolator, on the lower right corner of the cross-section as one looks downstream. The x-, y-, and z-coordinate directions are oriented in the direction of the bulk fluid flow, parallel to the 50.80 mm wall, and parallel to the 25.40 mm wall, respectively. Downstream of the isolator are two expansion sections with circular cross-sections of different diameters. The second expansion section contains a remotely controlled back pressure plug that translates in the x-direction. Translating this conical plug upstream toward the smaller diameter expansion section mechanically restricts the airflow area. This process increases the back pressure to emulate scramjet combustor conditions. As a result, a shock train is produced in the isolator. The second expansion section is followed by an exhaust duct that directs the air to the outside atmosphere.

To examine the highly three-dimensional shock train structure, FRS measurements are desired on multiple cross-sectional planes of the isolator. Figure 4 schematically represents the proposed optical arrangement. A custom Continuum Macropulse laser will be used to produce linearly polarized green light with a central frequency of

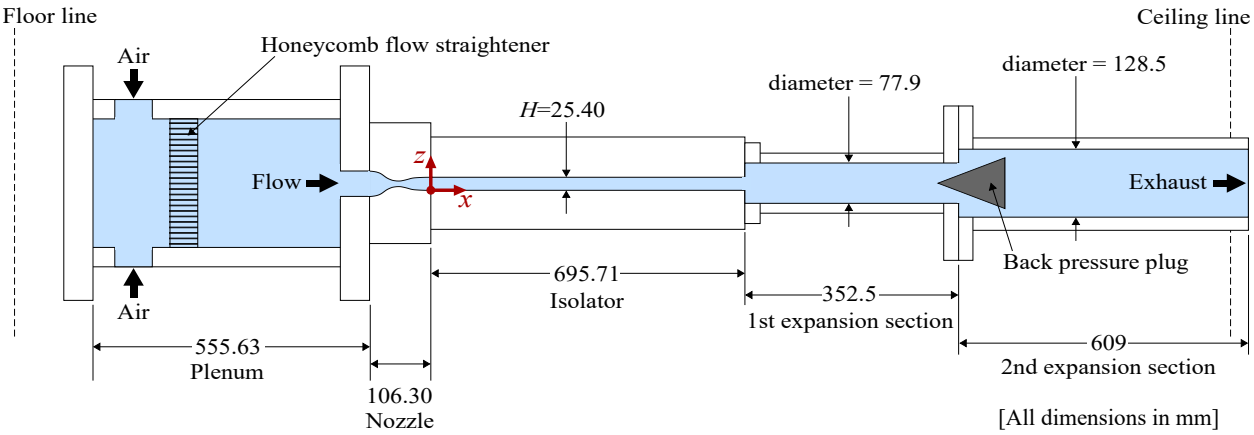

Fig. 3 Schematic diagram of the IDRL.

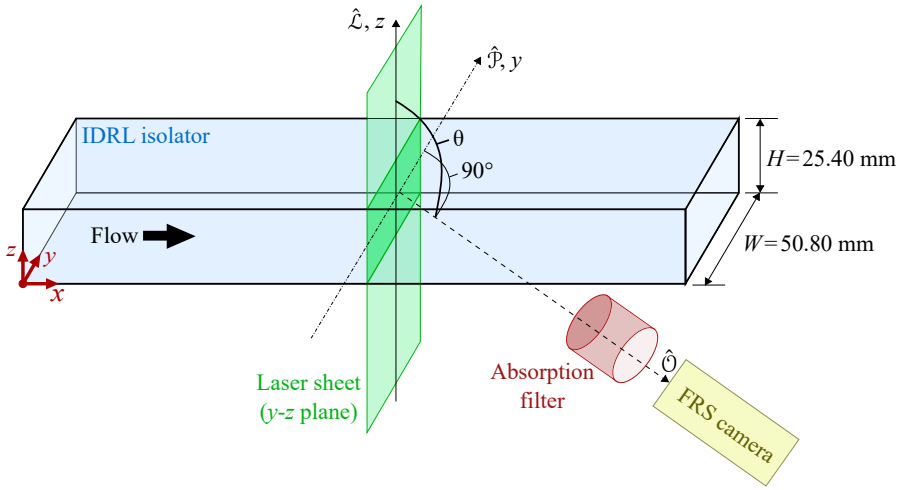

Fig. 4 Schematic diagram of the proposed FRS setup in the IDRL isolator. The laser sheet illuminates a cross-sectional y-z plane and the camera views the flow through a window in the x-y plane.

approximately 563.1 THz (18784 1/cm). An injection seeder will precisely tune the laser output to the desired frequency. This capability allows the laser output to be matched with the frequency of the chosen iodine absorption line so that the incident laser light and background scattering are filtered out of the measurements. Preliminary evaluations of the laser indicate that its spectral linewidth, defined as the full width at half maximum (FWHM), is approximately 90 MHz (0.003 1/cm). The laser light will be directed such that it propagates in the z-direction and thus, the polarization direction is in the x-y plane. The appropriate optics will be used to create a laser sheet that illuminates a y-z cross-sectional plane. A Princeton Instruments PhotonMAX EMCCD camera will image the RB scattered light after it passes through a molecular iodine absorption filter. The FRS camera will be located in the x-z plane at $y = H$ (i.e., the centerline of the tunnel width). It will be positioned an angle θ from the laser propagation direction and thus, the field of view will be distorted due to the angle of the camera. However, the image distortion can be corrected with proper calibration if the angle is not too severe. This camera position is selected so that the FRS setup only utilizes 2 parallel glass windows, leaving the other set of parallel walls open for additional diagnostics or instrumentation, such as wall static pressure ports.

IV. CFD of the IDRL Shock Train

Reynolds-Averaged Navier-Stokes (RANS) simulations of the IDRL shock train are used to evaluate if the proposed FRS experiment will result in adequate number density measurements. The CFD simulation was previously conducted by Baurle et al. [1] given the facility geometry and target plenum conditions. All computational results were obtained using the VULCAN-CFD (Viscous Upwind aLgorithm for Complex flow ANalysis) Navier-Stokes code developed and maintained by researchers in the Hypersonic Airbreathing Propulsion Branch at the NASA Langley Research Center. Specifically, CFD data was acquired by integrating the RANS equations until steady-state conditions were achieved. Refer to [1] for additional details on the CFD calculations. Examples of the CFD number density (N), pressure (p), and temperature (T) are shown in figure 5. Note these flow properties are normalized by the respective isolator inflow value ($N_{\text{inf}} = 2.88 \times 10^{19}$ cm^{-3}, $p_{\text{inf}} = 53.75$ kPa, and $T_{\text{inf}} = 134.92$ K). In each subfigure, the top contour map shows the streamwise x-y plane at $z = H/2$ (i.e., the centerplane). The bottom contour maps show cross-sectional planes at $x = 9.3H$, $x = 9.9H$, and $x = 10.5H$. For these calculations, the stagnation pressure and temperature are 861.850 kPa ($8.5p_{\text{atm}}$) and 298.15 K ($1.0T_{\text{atm}}$), respectively. The back pressure, defined at $x/H = 24$, is equal to 296.505 kPa ($2.9p_{\text{atm}}$).

V. Physics-Based Model for Predicting the Collected Radiant Energy Using CFD

The procedure described in this section is used to predict the total radiant energy that reaches the FRS camera, E, based on the optical setup mentioned in section III and the scattering gas properties (N, p, T, $\vec{v}$) provided by CFD. First, it is assumed that the background interference is mostly removed by the iodine filter. Thus, E_b has a negligible contribution to E and is defined to be zero for simplicity. Second, it is assumed that B, ℓ, E_i, and $\Delta\Omega$ are constant for all measurements because the optical setup does not change. Thus, the ratio of two radiant energy measurements is independent of these parameters. Here, the wind-on measurement, E, is normalized by the wind-off radiant energy of the RB scattering from stagnant air at atmospheric room conditions, E_{atm}. E_{atm} is chosen to normalize the other radiant energy measurements because it can be easily and accurately acquired prior to each run. The ratio of measurements is as follows:

$$\frac{E}{E_{\text{atm}}} = \frac{N\frac{\mathrm{d}\sigma}{\mathrm{d}\Omega}\int_{-\infty}^{+\infty} tr\,\mathrm{d}\nu}{\left[N\frac{\mathrm{d}\sigma}{\mathrm{d}\Omega}\int_{-\infty}^{+\infty} tr\,\mathrm{d}\nu\right]_{\text{atm}}} \tag{4}$$

The remaining discussion in this section outlines how the quantities $\mathrm{d}\sigma/\mathrm{d}\Omega$, t, and r are modeled.

The procedure of Forkey [6] is followed to calculate $\mathrm{d}\sigma/\mathrm{d}\Omega$. In the proposed coordinate system (see section III), the laser propagates in the z-direction and the observation direction is confined to the x-z plane (i.e., perpendicular to the y-axis). Note that this coordinate system can be uniquely defined for any arbitrary $\hat{\mathcal{L}}$ and $\hat{\mathcal{O}}$ directions. From the preselected equipment, it is also given that the incident laser light is linearly polarized and the CCD sensor is polarization insensitive. Under these conditions, the differential scattering cross section is equal to

$$\frac{\mathrm{d}\sigma}{\mathrm{d}\Omega} = \frac{\pi^2\nu_c^4(n-1)^2}{c^4N^2}\left[\frac{6+3\rho_0}{(6-7\rho_0)(2+\rho_0)}\right]\left[2\rho_0 + (8-9\rho_0)sin^2\phi\right] \tag{5}$$

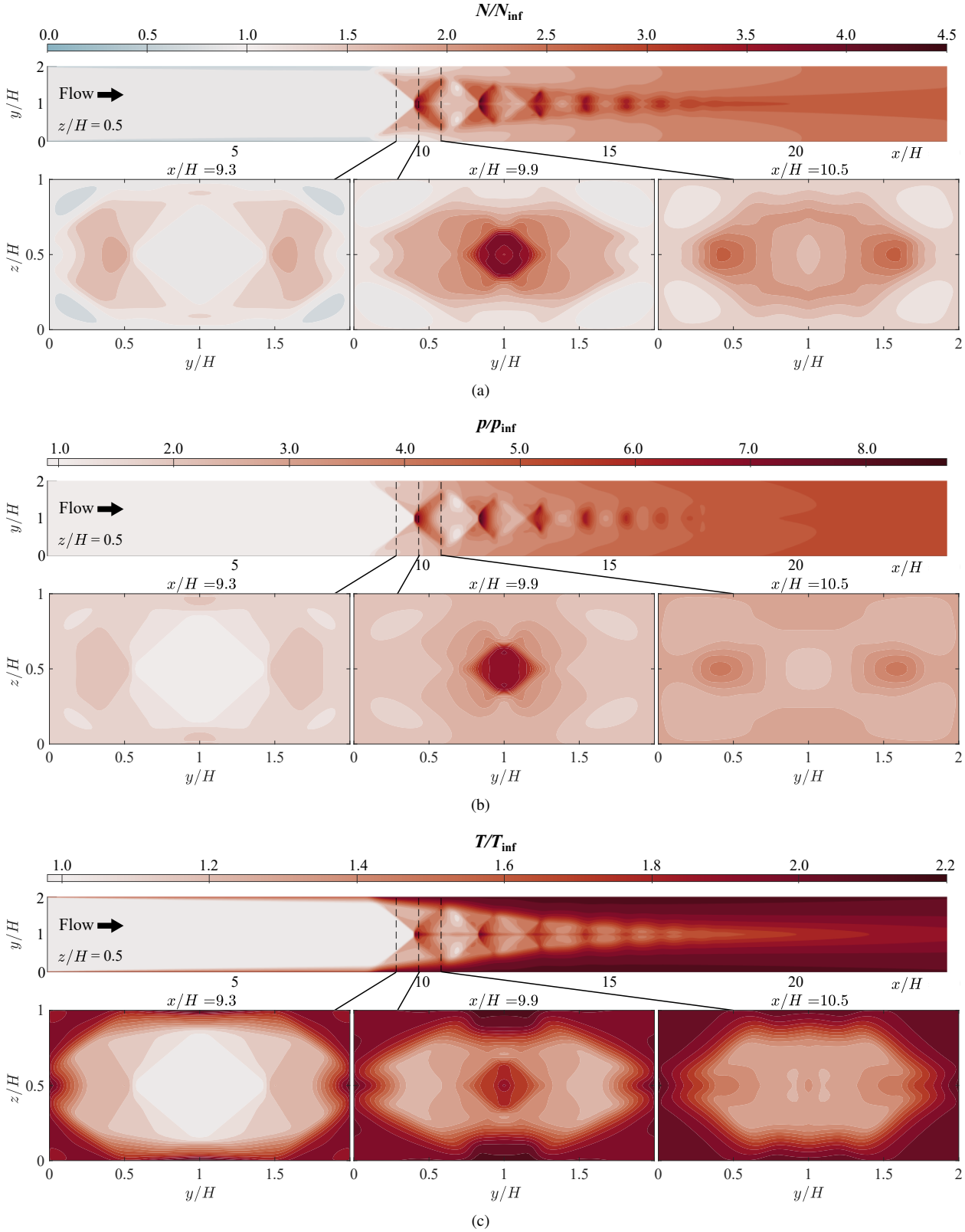

Fig. 5 CFD contour maps of flow properties normalized by their respective isolator inflow values: (a) number density; (b) pressure; (c) temperature. Top contour map of each subfigure shows the streamwise x-y plane at $z = H/2$ (i.e., the centerplane). Bottom contour maps show cross-sectional y-z planes at different x-locations.

where ϕ is the angle between $\hat{\mathcal{O}}$ and $\hat{\mathcal{P}}$. To maximize the measured signal, ϕ is defined to be 90° in this work (i.e., $\hat{\mathcal{P}}$ is parallel to the y-axis). For an incident laser wavelength of approximately 532 nm, ρ_0 is equal to 0.028 [6]. The number density is known from CFD and the index of refraction for air is calculated using the Ciddor equations [7]. Thus, $\mathrm{d}\sigma/\mathrm{d}\Omega$ is completely defined. However, equation 5 neglects the contribution due to the Stokes and anti-Stokes branches of pure rotational Raman scattering because the contribution is known to be small and difficult to model.

The transmission spectrum of the iodine absorption filter, t, is calculated using the model of Forkey et al. [8] with P_{cell}, T_{cell}, and L_{cell} values as inputs. Example transmission spectra for a small frequency range are shown in figure

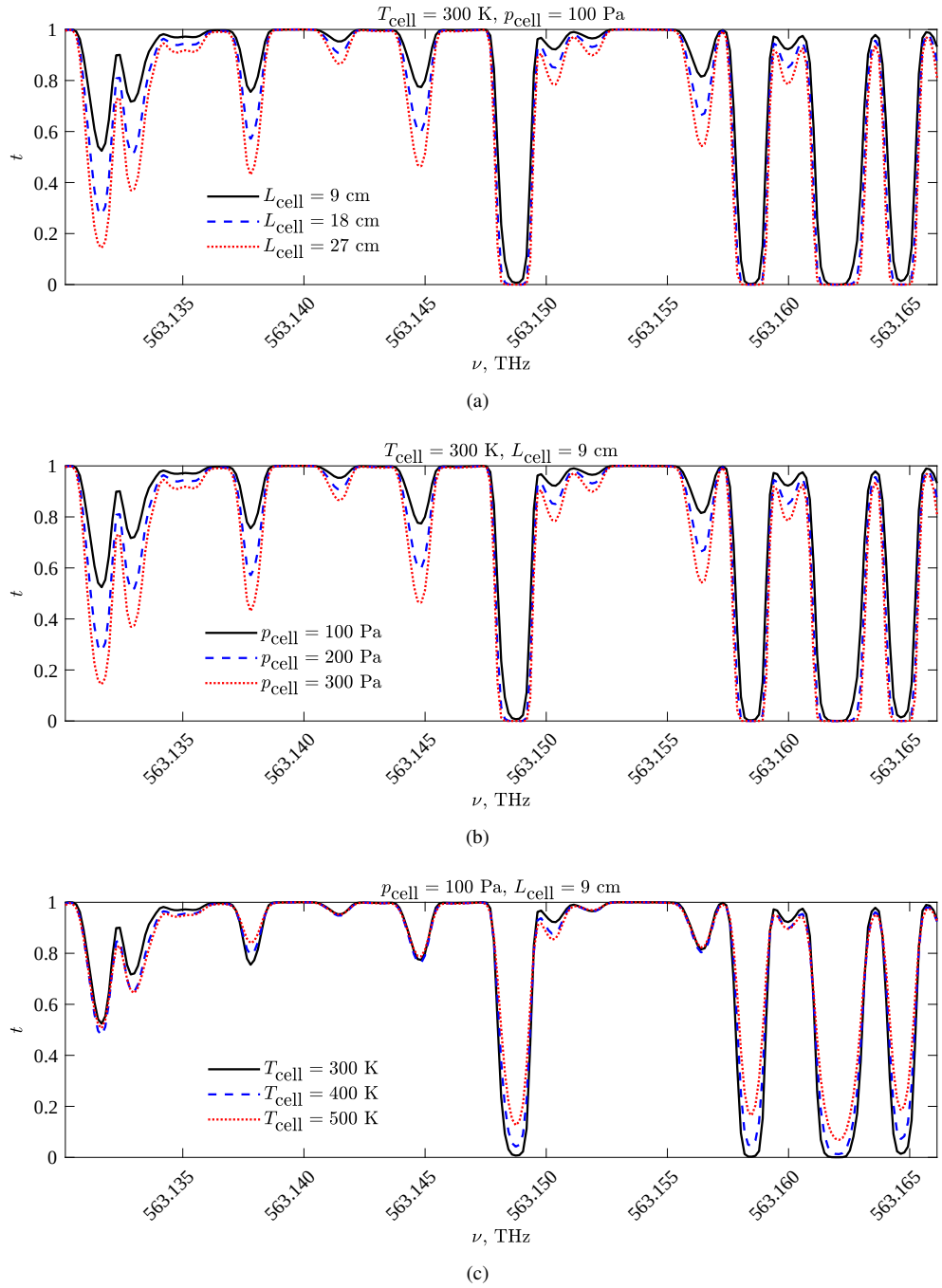

Fig. 6 Examples of how the transmission spectrum for an iodine filter changes with: (a) cell length; (b) cell pressure; (c) cell temperature.

6. Parts (a), (b), and (c) of the figure show how the absorption spectrum changes with filter length, pressure, and temperature, respectively. All three of these gas cell properties affect the minimum normalized transmission value and the linewidth but do not shift the center frequency of the absorption line. In this work, P_{cell}, T_{cell}, and L_{cell} are selected to be 100 Pa, 300 K, and 9 cm, respectively, because these values are representative of commercially available iodine absorption filters. In addition, the absorption line centered at approximately 563.148 THz is selected for several reasons: (1) the incident laser light is tunable at this wavenumber while maintaining sufficient laser power, (2) the absorption line is relatively strong for typical gas cell conditions (i.e., the minimum normalized transmission value is low) so most of the incident laser light and unwanted background light can be filtered out, (3) the absorption line is relatively narrow so it does not filter a large portion of the RB scattered light, and (4) the absorption line is relatively isolated so that the RB scattered light is not unnecessarily filtered by other absorption lines when it is Doppler shifted. Generally, the selected absorption line and gas cell properties are arbitrary because different cell properties could be chosen to generate an absorption line with the same qualities described above.

Lastly, a model for the RB scattering lineshape, r, is needed to compute the collected energy ratio, E/E_{atm}. Tenti's S6 model [9] is regarded as one of the most accurate physics-based models for r [10–12]. However, the Tenti model is computationally expensive and an impractical tool for computing the lineshape at each of the 33 million points contained in the IDRL shock train CFD grid. Instead, a procedure similar to that of Binietoglou et al. [13] is used to generate a linear approximation of the Tenti model based on Principal Component Analysis (PCA). First, a set of reference RB scattering spectra is computed with Tenti's S6 model given various scattering gas properties from CFD (i.e., $\vec{v}$, p, T, m, η, η_b, k, c_{int}, c_{tr}) and different experimental conditions (i.e., θ and ν_c). Note that these Tenti model inputs are evenly distributed across their expected range to ensure that the reference dataset encompasses all possible IDRL lineshapes. PCA on the reference dataset results in: (1) a mean lineshape, (2) a set of basis functions, i.e., principal components, and (3) a weighting matrix. For a given set of scattering gas properties and experimental conditions, the corresponding weights can be multiplied with the principal components and then added to the mean lineshape to exactly reconstruct the RB scattering lineshapes within the reference dataset. If only the five most dominant principal components are used, the reconstructed lineshape differs from the corresponding Tenti spectra by typically less than 0.5% at each frequency. Thus, these select components sufficiently represent the Tenti model lineshape and this reduced subset is used to reconstruct spectra with minimal computational effort. Next, a stepwise linear regression procedure is used to find polynomial expressions that relate the weights of the first five principal components to the input parameters. These polynomial fits are used to approximate the RB scattering lineshapes not contained in the reference dataset. This linear approximation retains the high accuracy of the Tenti model because the polynomial fits for the weights of the five principal components have a goodness-of-fit parameter greater than $R^2 = 0.998$.

As an example of the procedure discussed in this section, E/E_{atm} is calculated at each point in the CFD grid for a case where the experimental parameters θ and ν_c are selected to be 135° and 563.1486 THz (18784.614 1/cm), respectively. It is also assumed that the camera is sufficiently far away from the imaging region such that the pixel-to-pixel variations in θ and ϕ are negligible. Therefore, the average angular values are used for all energy calculations across the entire imaging plane. Several computational flow images (CFI) of this example case are presented in figure 7. Recall that the proposed experiment measures the scattered light intensity on a cross-sectional plane. Thus, the 2D cross-sectional images at the bottom of figure 7 predict what the camera would capture (after perspective correction) at different x-locations in the isolator. The streamwise x-y plane at the top of the figure is simply an informative image used for reference.

Notice that the contour plots of E/E_{atm} in figure 7 are slightly asymmetric about $z = H/2$ despite the fact that the two-sided facility nozzle is designed to produce flow in the isolator that is symmetric about both $y = H$ and $z = H/2$ centerplanes. This effect is caused by the asymmetry in Doppler shift. For the camera orientation described in section III, the Doppler shift is dependent on the velocity of the scattering gas in the the x- and z-directions, with the weighting of each component determined by θ (see equation 3 where θ is the angle between $\mathcal{O}$ and $\mathcal{L}$). Since the sign of the z-velocity component reverses across $z = H/2$, it follows that the Doppler shift is also asymmetric about this axis. As an example, figure 8 shows contour plots of the Doppler shift for the chosen θ value of 135°. The spectrum of the RB scattered light is shifted to a higher or lower frequency relative to the incident laser light for positive and negative Doppler shifts, respectively. Thus, changing the Doppler shift affects the amount of RB scattered light that is filtered by the absorption cell, leading to the asymmetry in E/E_{atm}.

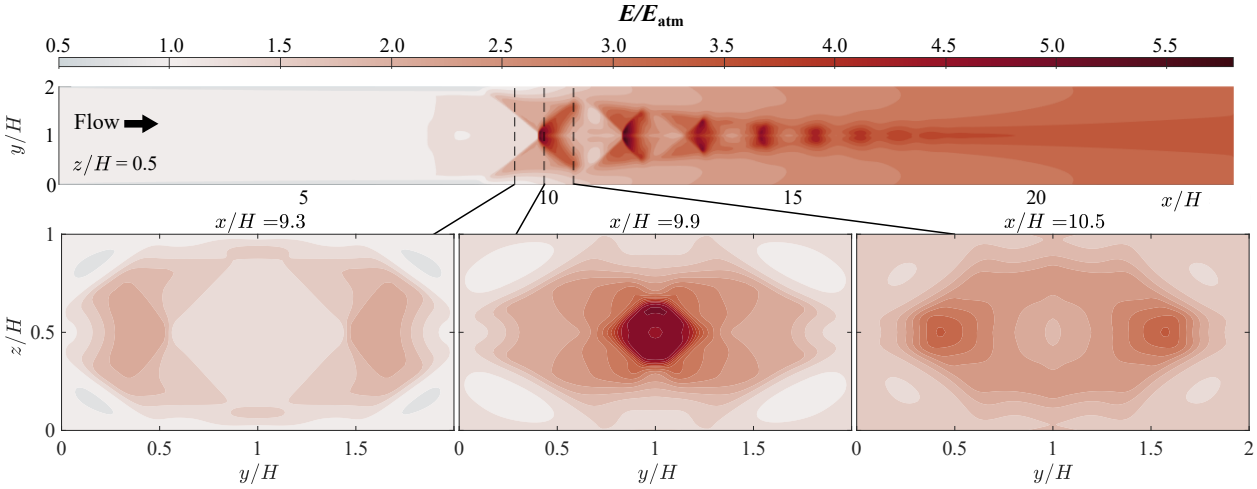

Fig. 7 Computational flow images of the collected radiant energy ratio. The top contour map shows the streamwise x-y plane at $z = H/2$ (i.e., the centerplane). The bottom contour maps show cross-sectional y-z planes at different x-locations. Calculations are made using $\theta = 135°$ and $\nu_c = 563.1486$ THz.

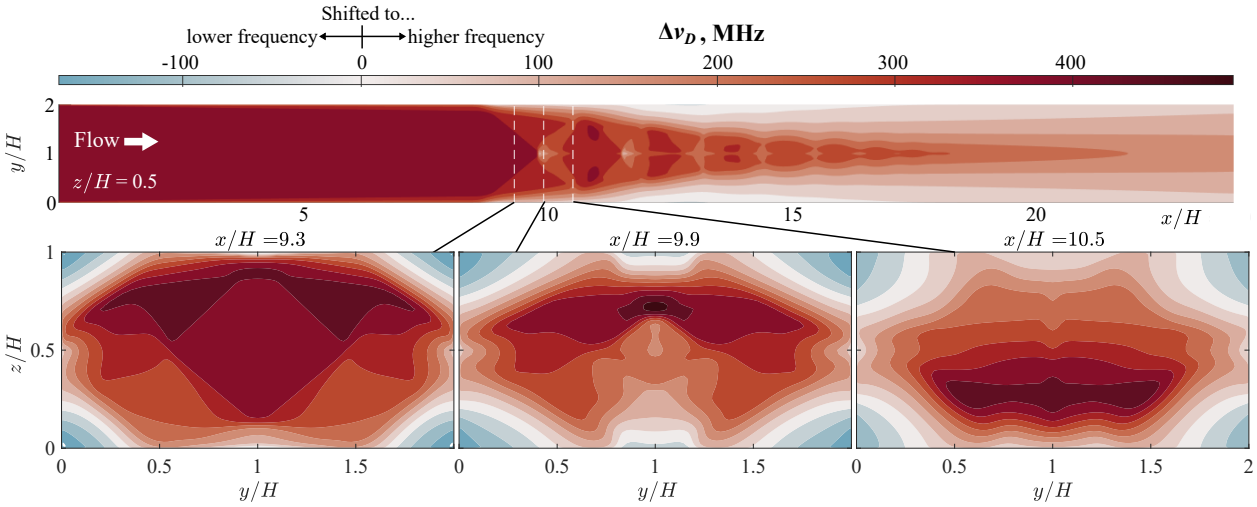

Fig. 8 Contour plots of the Doppler shift for $\theta = 135°$. The top contour map shows the streamwise x-y plane at $z = H/2$ (i.e., the centerplane). The bottom contour maps show cross-sectional y-z planes at different x-locations.

VI. Relationship Between Collected Radiant Energy and Number Density

In the previous section, flow field properties computed with CFD were input into a physics-based model to predict the collected energy ratio, E/E_{atm}. However, the opposite problem is worked in a typical experiment, where E/E_{atm} is measured and the goal is to extract flow field properties. In this section, a relationship between the number density of the scattering gas, N, and the collected energy ratio is established using the CFI calculated with the physics-based model described in section V. If the relationship sufficiently describes the number density across the entire flow field, it can be used in future experiments to determine N based on FRS measurements without any other information.

Consider the example presented at the end of the previous section where $\theta = 135°$ and $\nu_c = 563.1486$ THz (18784.614 1/cm). Figure 9 is a scatter plot of the normalized number density from CFD versus the collected energy ratio computed via the physics-based model for all points in the full three-dimensional CFD matrix, including the freestream flow. The red curve is a simple linear fit through the point cloud. In this work, the "true" number density is the CFD value. However, the linear fit can be interpolated for any given E/E_{atm} value to find the "predicted" number density. The true and predicted normalized number densities for a streamwise x-y plane at $z = H/2$ are compared side by side using the top and middle contour plots in figure 10. The bottom contour plot in the figure shows the prediction

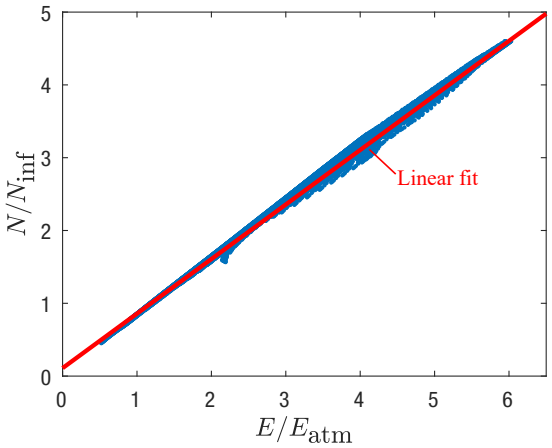

Fig. 9 Normalized number density from CFD versus energy ratio computed via the physics-based model for all points in the CFD matrix. Calculations made using $\theta = 135°$ and $\nu_c = 563.1486$ THz.

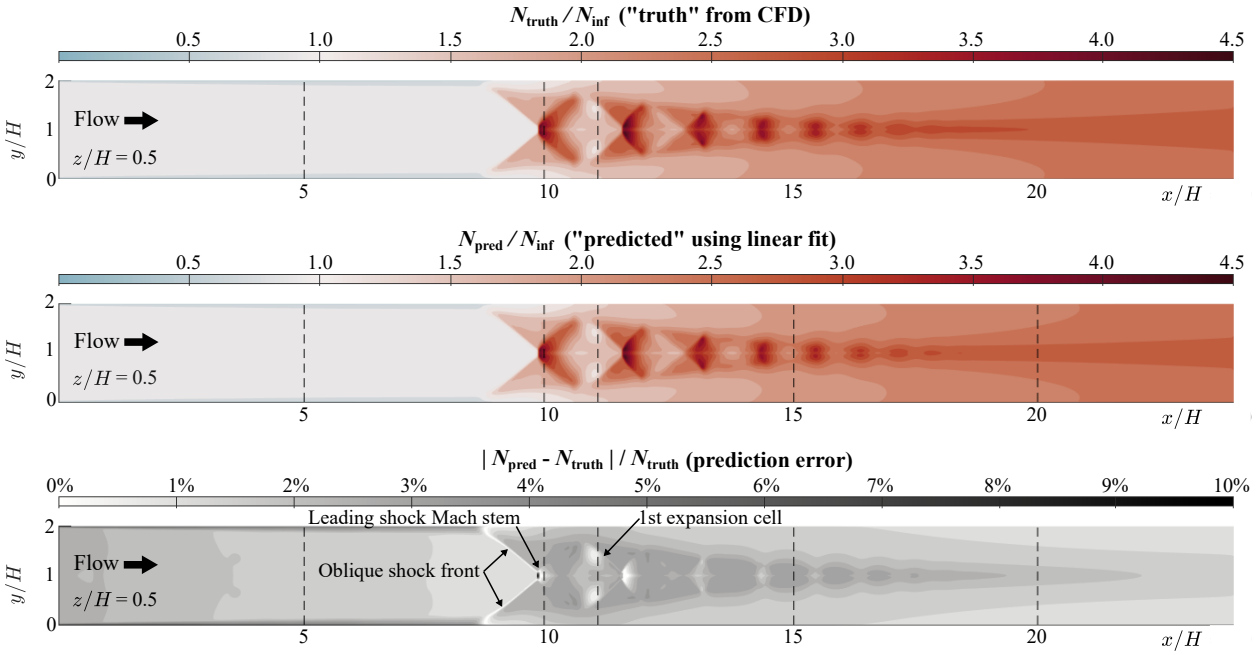

Fig. 10 Contour maps of the streamwise x-y plane at $z = H/2$ (i.e., the centerplane). Top: True normalized number density. Middle: Predicted normalized number density. Bottom: Absolute value of the prediction error. Calculations are made using $\theta = 135°$ and $\nu_c = 563.1486$ THz.

error, defined as $|N_{\mathrm{pred}} - N_{\mathrm{truth}}|/N_{\mathrm{truth}}$, in terms of percentages. Similarly, the first two columns in figure 11 show the true and predicted normalized number density for cross-sectional planes at $x/H = 5.0$, 9.9, 11.0, 15.0, and 20.0. The last column shows the corresponding prediction error for each plane. Note that the vertical dashed lines in figure 10 illustrate the axial locations of the cross-sectional planes shown in figure 11.

Both figure 10 and 11 demonstrate that the chosen linear fit accurately describes the number density of the flow. The lowest prediction errors occur at the oblique shock front of the first shock structure and the first expansion cell (see labels in figure 10). In these regions, the percent error is less than 1%. In contrast, the Mach stem of the leading

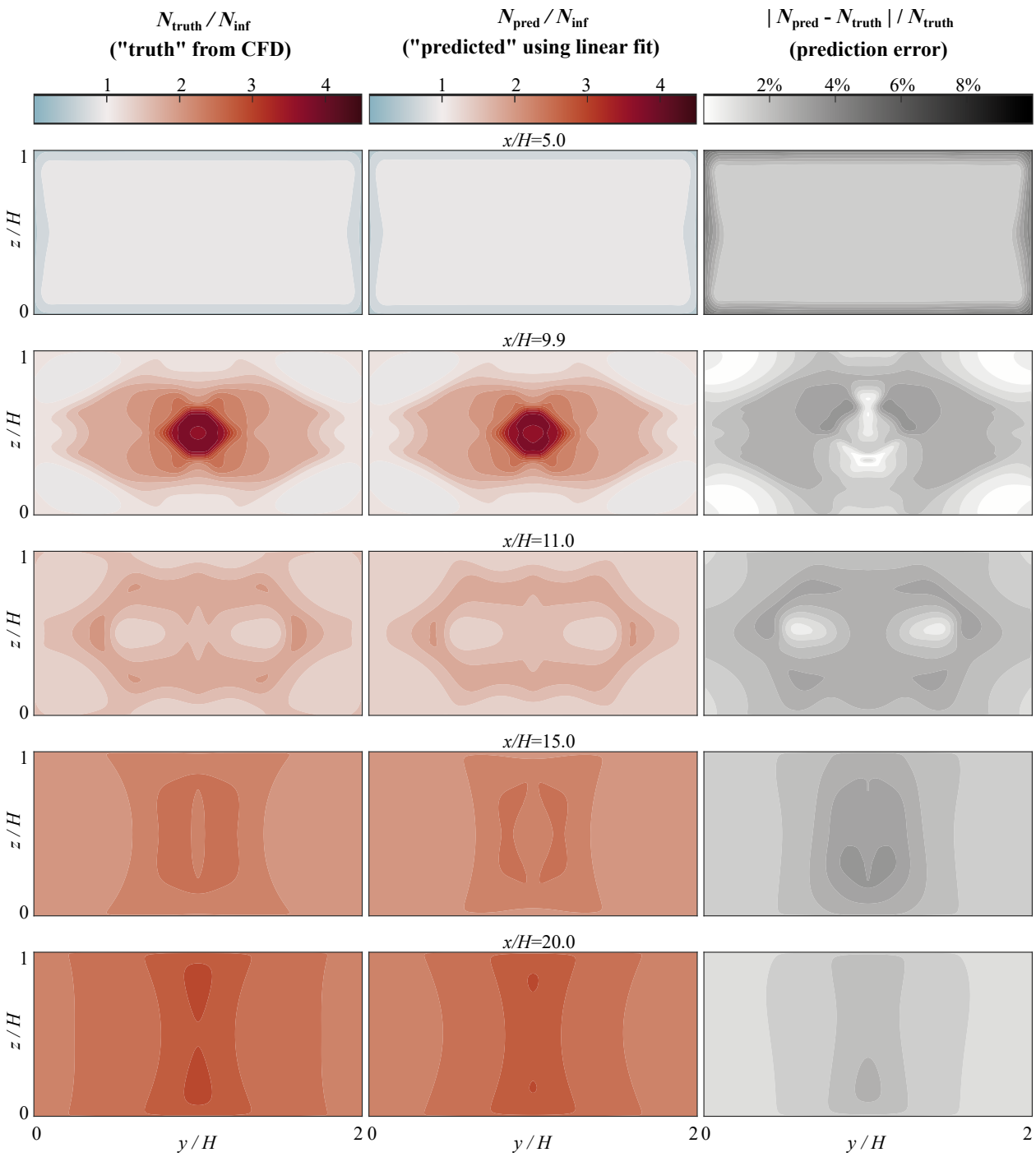

Fig. 11 Contour maps of cross-sectional y-z planes at different x-locations. Left: True normalized number density. Middle: Predicted normalized number density. Right: Absolute value of the prediction error. Calculations are made using $\theta = 135°$ and $\nu_c = 563.1486$ THz.

shock (see label in figure 10) exhibits the largest prediction error of 11%. However, these high errors are limited to a spatially small region in the flow field. In the freestream flow, the low momentum boundary layer very close to the wall exhibits moderate prediction error (up to 7%), but once again, this is a spatially small region. Figure 12 shows the probability distribution of the number density prediction error across the full three-dimensional CFD matrix. This figure demonstrates that the vast majority of the flow field exhibits small prediction errors that are less than 4%. The mean and

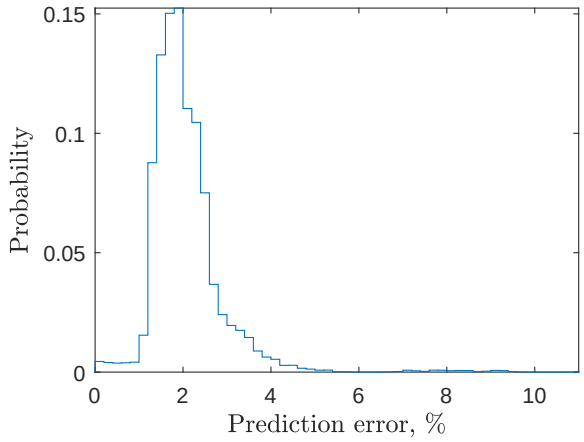

Fig. 12 Histogram of the number density prediction error. Calculations made using $\theta = 135°$ and $\nu_c = 563.1486$ THz.

median prediction errors are both approximately 2%. In an actual experiment, the total error will have contributions from the linear fit prediction as well as other measurement errors, such as (but not limited to) residual scattered light interference, shot noise, and uncertainty in the laser linewidth. Starting with a low prediction error from the fitting process is a good indication that the proposed FRS setup can be used to accurately quantify number density in the IDRL isolator despite the fact that the scattered light intensity depends on many parameters.

VII. Sensitivity Analysis: How Experimental Parameters Impact Prediction Error

Thus far, results have only been presented for one specific combination of θ and ν_c. It is found that this selection is optimal for this particular IDRL experiment, but in general, these parameters can be varied to alter the number density prediction error. Table 1 describes eight cases with different parameters defining the experimental setup that will be examined in this section. Cases 1, 2, 3, and 5 have the same value of θ, but ν_c is varied from 563.1485 to 563.1491 THz. Cases 4–8 have the same ν_c, but vary θ from 45 to 160 degrees. For reference, case 7 is the optimal case discussed in the previous section and described using figures 7 – 11.

First, consider cases 1, 2, 3, and 5 where ν_c is varied while holding the camera angle constant at 100 degrees. Since the gas properties in the absorption filter are the same for all of these calculations, changing ν_c moves the center of the laser's spectral profile to a different position in the absorption line as demonstrated by figure 13. For reference, the laser line in case 3 is positioned near the edge of the absorption line on the low-frequency side. The normalized filter transmission is non-zero for part of the incident light spectrum which results in approximately 2.0% unfiltered

Table 1 Summary of cases analyzed in the sensitivity analysis.

Case	θ, degrees	ν_c, THz	Unfiltered light, %	Mean prediction error, %	Max prediction error, %
1	100	563.1485	3.7	4.3	14.5
2	100	563.1488	0.7	11.8	27.2
3	100	563.1491	2.0	15.9	30.6
4	45	563.1486	1.9	51.7	104.9
5	100	563.1486	1.9	5.2	22.0
6	118	563.1486	1.9	2.6	12.8
7*	135	563.1486	1.9	2.1	11.8
8	160	563.1486	1.9	2.0	12.4

* Optimal case described in section VI using figures 7 – 12

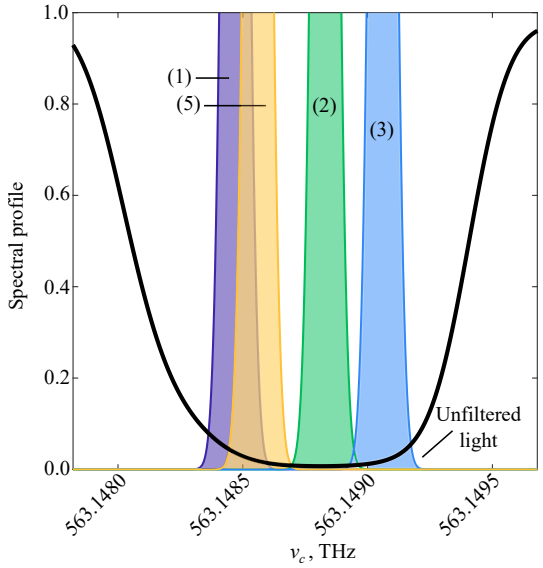

Fig. 13 Spectral profile of the iodine filter transmission (black curve) and the incident laser light (color curves) for cases 1, 2, 3, and 5.

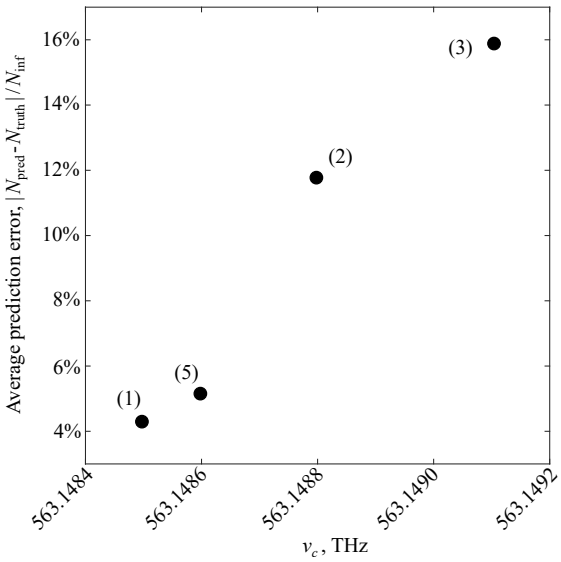

Fig. 14 Average number density prediction error versus the central frequency of the incident laser light for cases 1, 2, 3, and 5.

incident laser light in this case. Case 1 is an example of the other extreme, where the laser line is positioned on the high-frequency side of the absorption line. Here, 3.7% of the incident laser light is unfiltered. As demonstrated by figure 14, the average number density prediction error increases with ν_c. Thus, positioning the incident laser line on the low-frequency side of the absorption line is desired for low prediction errors, but this must be balanced with the amount of unfiltered incident laser light as it will produce detrimental background interference.

The trend in average prediction error versus ν_c was not readily apparent before conducting the sensitivity analysis. Often, experiments on flow fields with large Doppler shifts are conducted such that the incident laser light is positioned on the side of the absorption line that corresponds to the direction of the Doppler shift. If the Doppler shift is large enough, the RB scattering spectrum does not overlap the absorption line and this light is not filtered at all, making the measured energy ratio have a direct dependence on number density. In other words, the integral term in equation 2 is equal to one. This approach does not work for the current experiment because the flow exhibits a large range of both positive and negative Doppler shifts. Instead, the incident laser light should be positioned relative to the absorption line such that the effect of Doppler shift is minimized. Ideally, the same amount of the RB scattered light is filtered by the absorption cell at all points in the flow field. That is, the integral term in equation 2 is a constant less than one. For the lowest ν_c case presented in this work (i.e., case 1), the integral term varies between 0.45 and 0.58 across the entire flow field, thus yielding a range of 0.13. While the integral term is not exactly constant, it has a small enough range to support low number density prediction errors. In comparison, the prediction error is higher for case 3 (i.e., the highest ν_c case) because the integral term varies between 0.46 and 0.76, thus yielding a range of 0.30.

Based on similar reasoning, increasing θ improves the number density prediction error as follows. The streamwise component of velocity contributes less to the Doppler shift as θ increases. Since the streamwise component of velocity can be an order of magnitude greater than the transverse velocity components in an isolator shock train, the Doppler shift magnitude rapidly decreases with increasing θ. The smaller magnitude in Doppler shift means that the RB scattering spectrum does not shift as much relative to the incident laser light or the absorption line. As a result, the integral term in equation 2 has a smaller range across the entire flow field and the proposed technique becomes more of a direct measurement of number density. For instance, the integral term varies between 0.53 and 0.61 (i.e., a range of 0.08) for the optimal case 7 where $\theta = 135°$. In comparison, the integral term varies between 0.12 and 0.44 (i.e., a range of 0.32) for case 4 where $\theta = 45°$. To summarize, increasing θ reduces the measurement sensitivity to Doppler shift, thus reducing the prediction error. Figure 14 illustrates the resulting decrease in number density prediction error as θ goes from 45° – 160° in cases 4 – 8.

The experimental parameters of case 7 are chosen as the optimal conditions to use in a future experiment based on a compromise between number density prediction error, spatial resolution, and the amount of unfiltered light. While

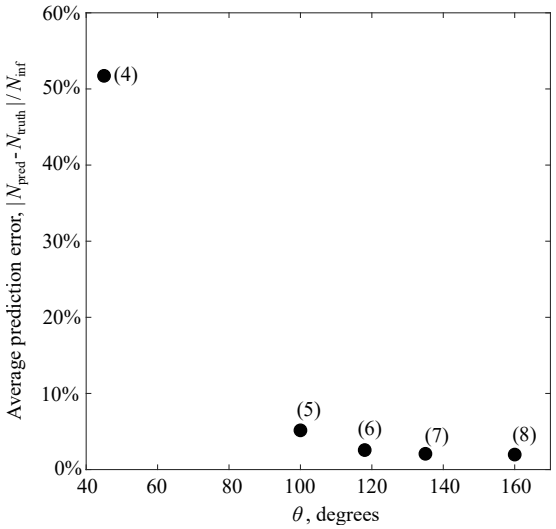

Fig. 15 Average number density prediction error versus the camera angle, θ, for cases 4 – 8.

the lowest possible ν_c value is desired to reduce prediction errors, ν_c must also be located relative to the absorption line such that an acceptably small amount of light is unfiltered. Thus, excessive background scattering off the facility windows and structural frame is avoided. For this work, 2% unfiltered light is assumed to be the maximum value for adequate measurements. This will have to be validated in an actual experiment. However, ν_c can be shifted to a slightly higher value without drastically increasing the prediction error. A large value of θ is also desired for small prediction errors, but this choice also means that the imaging plane will be viewed at a severe angle. The perspective distortion can be corrected with proper camera calibration, for example, using a dot card or grid pattern to find the intrinsic camera parameters which are then used to adjust the FRS images in a post-processing step. However, a high θ value reduces the spatial resolution in the z-direction. Since number density prediction error is not very sensitive to θ from 120° to 160°, an optimal θ value of 135° is selected. That is, the camera is at a 45° angle from the imaging plane.

VIII. Conclusion

FRS is a suggested quantitative measurement capability for future experiments in the IDRL because it can provide spatially- and temporally-resolved quantitative data on an imaging plane without intrusively seeding the flow. This allows detailed studies into the complex three-dimensional shock train structure. While the absorption filter used in this diagnostic introduces a signal dependence on many flow properties, the small-scale and enclosed nature of the facility necessitates a filter to remove the background interference which overwhelms the relatively weak signal from the scattering gas. In this work, the feasibility of using a simple FRS experiment (comprised of a single camera, laser, and absorption filter) to measure number density in the isolator shock train flow field was evaluated. To do so, CFD simulations of the shock train were input into a physics-based model to predict the amount of collected radiant energy. Based on a sensitivity analysis conducted, it was found that certain parameters for the experimental setup can be chosen such that number density is well described by a linear relationship with collected radiant energy. In future work, the proposed FRS experiment with a θ value of 135° and ν_c equal to 563.1486 THz will be explored experimentally. The chosen parameters strike a balance between minimizing the prediction error, maintaining a low amount of unfiltered light (approximately 2%), and acquiring images with high enough spatial resolution. Given these experimental parameters, the maximum expected error in the number density prediction is approximately 11%. However, high prediction errors are limited to a small region of the flow near the leading shock Mach stem. The mean and median prediction errors across the entire flow field are both approximately 2%. Thus, the majority of the flow field is deemed to have a sufficiently small amount of error for quantitative measurements that can be used to describe the flow field physics and validate CFD simulations.

Acknowledgments

Funding for this effort was provided by the NASA Hypersonic Technology Project under the Advanced Air Vehicles Program of the Aeronautics Research Mission Directorate. The authors would like to thank Dr. Austin Ziltz and Dr. Tomasz Drozda for the valuable discussions regarding this work.

References

[1] Baurle, R. A., Middleton, T. F., and Wilson, L. G., "Reynolds-Averaged Turbulence Model Assessment for a Highly Back-Pressured Isolator Flowfield," *JANNAF 33rd Airbreathing Propulsion Subcommitte Meeting*, 2012, pp. 1–23.

[2] Koo, H., and Raman, V., "Large-Eddy Simulation of a Supersonic Inlet-Isolator," *AIAA Journal*, Vol. 50, No. 7, 2012, pp. 1596–1613.

[3] Fievet, R., "Impact of Vibrational Nonequilibrium on the Simulation and Modeling of Dual-Mode Scramjets," Ph.D. thesis, University of Michigan, Ann Arbor, MI, 2018.

[4] Lindstrom, C. D., Jackson, K. R., Williams, S., Givens, R., Bailey, W. F., Tam, C.-J., and Terry, W. F., "Shock-Train Structure Resolved with Absorption Spectroscopy Part 1: System Design and Validation," *AIAA Journal*, Vol. 47, No. 10, 2009, pp. 2368–2378.

[5] Hunt, R. L., and Gamba, M., "Shock Train Unsteadiness Characteristics, Oblique-to-Normal Transition, and Three-Dimensional Leading Shock Structure," *AIAA Journal*, Vol. 56, No. 4, 2018, pp. 1569–1587.

[6] Forkey, J. N., "Development and Demonstration of Filtered Rayleigh Scattering - A Laser Based Flow Diagnostic For Planar Measurement of Velocity, Temperature and Pressure," Ph.D. thesis, Princeton University, Princeton, NJ, 1996.

[7] Ciddor, P. E., "Refractive Index of Air: New Equations for the Visible and Near Infrared," *Applied Optics*, Vol. 35, No. 9, 1996, pp. 1566–1573.

[8] Forkey, J. N., Lempert, W. R., and Miles, R. B., "Corrected and Calibrated I2 Absorption Model at Frequency-Doubled Nd:YAG Laser Wavelengths," *Applied Optics*, Vol. 36, No. 27, 1997, pp. 6729–6738.

[9] Tenti, G., Boley, C. D., and Desai, R. C., "On the Kinetic Model Description of Rayleigh–Brillouin Scattering from Molecular Gases," *Canadian Journal of Physics*, Vol. 52, No. 4, 1974, pp. 285–290.

[10] Mcmanus, T. A., Monje, I. T., and Sutton, J. A., "Experimental Assessment of the Tenti S6 Model for Combustion-Relevant Gases and Filtered Rayleigh Scattering Applications," *Applied Physics B*, Vol. 125, No. 13, 2019, pp. 1–23.

[11] Witschas, B., Vieitez, M. O., van Duijn, E.-J., Reitebuch, O., van de Water, W., and Ubachs, W., "Spontaneous Rayleigh–Brillouin scattering of ultraviolet light in nitrogen, dry air, and moist air," *Applied Optics*, Vol. 49, No. 22, 2010, pp. 4217–4227.

[12] Vieitez, M. O., van Duijn, E. J., Ubachs, W., Witschas, B., Meijer, A., de Wijn, A. S., Dam, N. J., and van de Water, W., "Coherent and spontaneous Rayleigh-Brillouin scattering in atomic and molecular gases and gas mixtures," *Physical Review A*, Vol. 82, No. 043836, 2010, pp. 1–14.

[13] Binietoglou, I., Giampouras, P., and Belegante, L., "Linear Approximation of Rayleigh-Brillouin Scattering Spectra," *Applied Optics*, Vol. 55, No. 27, 2016, pp. 7707–7711.